
On the Sins of Image Synthesis Loss for Self-supervised Depth Estimation

Zhaoshuo Li, Nathan Drenkow, Hao Ding, Andy S. Ding, Alexander Lu,

Francis X. Creighton, Russell H. Taylor, Mathias Unberath
Johns Hopkins University

Abstract

Scene depth estimation from stereo and monocular imagery is critical for extracting 3D information for downstream tasks such as scene understanding. Recently, learning-based methods for depth estimation have received much attention due to their high performance and flexibility in hardware choice. However, collecting ground truth data for supervised training of these algorithms is costly or outright impossible. This circumstance suggests a need for alternative learning approaches that do not require corresponding depth measurements. Indeed, self-supervised learning of depth estimation provides an increasingly popular alternative. It is based on the idea that observed frames can be synthesized from neighboring frames if accurate depth of the scene is known – or in this case, estimated. We show empirically that – contrary to common belief – improvements in image synthesis do not necessitate improvement in depth estimation. Rather, optimizing for image synthesis can result in diverging performance with respect to the main prediction objective – depth. We attribute this diverging phenomenon to aleatoric uncertainties, which originate from data. Based on our experiments on four datasets (spanning street, indoor, and medical) and five architectures (monocular and stereo), we conclude that this diverging phenomenon is independent of the dataset domain and not mitigated by commonly used regularization techniques. To underscore the importance of this finding, we include a survey of methods which use image synthesis, totaling 127 papers over the last six years. This observed divergence has not been previously reported or studied in depth, suggesting room for future improvement of self-supervised approaches which might be impacted the finding.

1 Introduction

Depth estimation from images has long been recognized as an important research area and has gained substantial interest in recent years given its utility for downstream tasks such as scene understanding, registration, navigation, and control. Learning-based models often work well under strong supervision, but acquiring the necessary ground truth depth data can be cost prohibitive or impossible and often requires additional planning and extra hardware [9].

Self-supervised learning methods, which construct auxiliary objectives for training models, are often used to overcome the lack of ground truth depth information. Most work in self-supervised learning for depth estimation synthesizes images from different, but neighboring, viewpoints into one common frame, given estimated depth and ego motion, and maximizes the similarity between observed and synthesized frames in place of ground truth supervision. The learning task is shown in Figure 1. Given a disparity prediction (which is proportional to inverse depth, we use the terms interchangeably) from a primary coordinate frame and relative camera pose, the image from a neighboring viewpoint is warped to the primary frame, followed by the computation of a synthesis loss based on the appearance

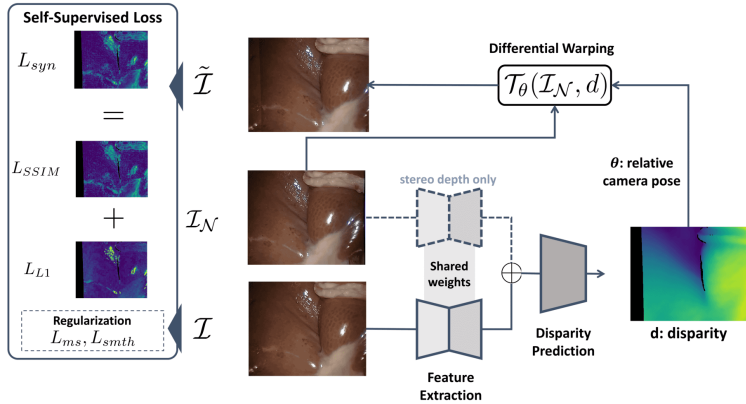


Figure 1: Overall process for self-supervised depth estimation using image synthesis. \mathcal{I} is the image of the primary frame. \mathcal{I}_N is the neighboring frame to generate the synthesized image $\tilde{\mathcal{I}}$ given the disparity estimation d and relative camera pose θ . In monocular depth networks, only \mathcal{I} is used to predict disparity. In stereo depth networks, both images are used to predict disparity.

difference between the observed and synthesized images. The ideas behind this self-supervised approach are valid given that neighboring frames only differ in viewpoint. This paradigm creates new opportunities to train depth estimation networks in previously data-constrained domains and has led to many top-performing self-supervised depth estimation networks [40, 10, 35].

However, during internal experimentation using the image synthesis loss for refining depth estimation networks after transfer to different data domains, we observed divergence (formal definition in Section 2.5) between performance on the surrogate (image synthesis) and true target objective (depth estimation). We observed that even if in some cases the networks final performance improved, optimization failed to stabilize for the most optimal operating point found; in other cases, the depth estimation performance of networks directly worsens as image synthesis improves. This circumstance is worrisome because in the faithful self-supervised learning setting, *where true depth measurements are unknown*, a well-intended attempt at improving depth estimation performance of a transferred model through fine-tuning using image synthesis may, in fact, result in the exact opposite: worsening of depth estimation performance. Therefore, in this paper, we raise the following questions:

1. *Is image synthesis effective as an auxiliary task for training deep depth estimation networks?* Yes, but only to a certain extent. We conduct extensive experiments using various contemporary networks on several datasets. We show in Section 4.1 that the gradient from image synthesis will actually *disagree* with that of the theoretically *unobserved* depth loss after a certain point. Thus, updating parameters in the negative gradient direction determined from the image synthesis loss will instead worsen depth prediction. The divergence is observed both at image-level and pixel-level (Section 4.2).
2. *Can perfect image synthesis be achieved from ground truth depth information?* In short, no. In Section 4.3, we demonstrate that even using the ground truth depth, image synthesis is far from perfect. This suggests that optimizing for image synthesis may indeed deviate from the true objective of depth estimation.
3. *What is behind the diverging phenomenon between image synthesis and depth estimation?* In Section 4.4, we analyze the loss manifold of image synthesis at places where we observe divergence. We show the disagreement between image synthesis loss and depth error, and the non-convexity of image synthesis loss at these places. We attribute the source of uncertainties to the data itself, also known as aleatoric uncertainty.
4. *What is the larger significance of this finding?* In Appendix I, we summarize a literature review following PRISMA guidelines [26] that resulted in 127 papers using image synthesis loss, or small variations thereof. None of these papers reported a diverging behaviour, which underscores the impact of the image synthesis paradigm on self-supervised depth estimation.

We hope that identifying this issue will enable further research on improving on the clearly impactful image synthesis paradigm for self-supervised training.

2 Background and Related Work

2.1 Learning-based Depth Estimation

Recently, deep learning has shown promising performance for depth estimation, where depth can be estimated from monocular image or stereo image pairs. In both cases, the depth estimation Z is calculated from the disparity estimation d , with $Z \propto 1/d$. Monocular depth networks rely on data priors to regress up-to-scale depth from a single image [5], *i.e.* the exact proportionality between depth and disparity are unknown; while stereo depth networks rely on pixel matching between image pairs to produce metric depth estimation [34], *i.e.* depth is found exactly with $Z = bf/d$, where b is the stereo baseline and f is the focal length. Both monocular and stereo networks can be trained in a self-supervised way using image synthesis (Figure 1).

To ensure that our findings regarding the image synthesis loss are not limited to a specific design of the network, we have selected a diverse set of architectures, including both monocular networks and stereo networks. Due to the high sensitivity to camera setup and scene variation for monocular depth networks [5], we only included the SOTA MonoDepth2 [10]. As stereo networks are better constrained in terms of depth estimation, we included several recent networks of different network design, including convolution networks MADNet [35], HSM [41], GwcNet [13], and a transformer network STTR [20]. We refer interested readers to Appendix A and the papers for more details.

2.2 Image Synthesis

As illustrated in Figure 1, a synthesized image $\tilde{\mathcal{I}}$ can be generated given the disparity, relative camera pose, and the image from a neighboring viewpoint \mathcal{I}_N . This can be achieved by either using images from concurrent observations from different cameras (*spatial stereo*), or a series of observations from the same camera (*temporal stereo*). In both cases, image synthesis is only valid for co-observed and static objects [10]. In our experiment, we only use the valid pixels and the ground truth camera poses to constrain the varying factor of image synthesis to be only the estimated disparity. To enable gradients to flow backwards through the disparity prediction to the network parameters, differentiable warping [16] is used for synthesizing images.

2.3 Self-supervised Training Using Image Synthesis for Depth Estimation

The most commonly used image synthesis loss was first proposed for image denoising and demosaicing tasks by Zhao *et al.* [43] and later adapted for depth estimation in Godard *et al* [9]. The loss itself is typically formulated as a weighted sum of structural similarity (SSIM) loss [38] and L1 loss between the observed and synthesized images, which can be written as

$$L_{syn} = \alpha L_{SSIM} + (1 - \alpha) L_{L1}, \quad (1)$$

$$L_{SSIM} = \frac{1}{2|\mathcal{N}|} \sum_{i \in \mathcal{N}} 1 - \frac{2\mu(\mathcal{I}_i)\mu(\tilde{\mathcal{I}}_i) + C_1}{\mu^2(\mathcal{I}_i) + \mu^2(\tilde{\mathcal{I}}_i) + C_1} \cdot \frac{2\sigma(\mathcal{I}_i)\sigma(\tilde{\mathcal{I}}_i) + C_2}{\sigma^2(\mathcal{I}_i) + \sigma^2(\tilde{\mathcal{I}}_i) + C_2}, \quad (2)$$

$$L_{L1} = \frac{1}{|\mathcal{N}|} \sum_{i \in \mathcal{N}} |\mathcal{I}_i - \tilde{\mathcal{I}}_i|. \quad (3)$$

$\mathcal{I}_i, \tilde{\mathcal{I}}_i$ are the i -th pixels in the total \mathcal{N} pixels. In Equation 2, μ and σ are the mean and standard deviation within a local patch, C_1 and C_2 are small constants to avoid division by 0. The synthesis loss is designed to measure both shape and appearance similarities. SSIM is mean balanced; therefore, it better preserves high frequency signals and is robust to chromatic differences. Conversely, L1 preserves color and luminance regardless of local structure. $\alpha \in [0, 1]$ is a weighting factor measuring the trade-off between the two loss terms.

2.4 Additional Regularization and Auxiliaries

It has previously been observed that L_{syn} suffers from a gradient locality problem, where both depth loss and L_{syn} stagnate, since it relies on the comparison of localized pixel intensities [32, 42]. Multi-scale regularization, *i.e.*, estimating disparities and computing L_{syn} at different spatial scales (L_{ms}), has been reported to mitigate the gradient locality problem [32, 9, 10]. Additionally, an edge-aware smoothness regularizing term L_{smth} on the disparity map has also been included [19, 35] to encourage smoothness of the estimation,

$$L_{smth} = \frac{1}{|\mathcal{N}|} \sum_{i \in \mathcal{N}} |\delta_x d_i| e^{-|\delta_x \mathcal{I}_i|} + |\delta_y d_i| e^{-|\delta_y \mathcal{I}_i|}. \quad (4)$$

Here d is the estimated disparity map, and δ denotes first order gradient. Due to the popularity of these two regularization approaches, we conduct additional experiments and show in Appendix B neither of these regularization approaches prevents the divergent phenomenon observed (often only mitigating it to a negligible extent).

Other auxiliary techniques to L_{syn} have also been proposed. For example, [37] uses deep reinforcement learning to decide if the gradient computed from L_{syn} for a specific stereo pair of images should back-propagate to the network. In [44], a recurrent neural network is used to backpropagate the gradient of L_{syn} conditioned on a sequence of past frames. We do not consider these works in our experiments because they add additional sophistication and challenges associated that would be conflated with the divergence issue under examination.

2.5 Divergence and Spearman’s Rank Coefficients

In our experiment, we report the accuracy of disparity estimation via end-point-error (EPE), *i.e.*, the absolute disparity error. Since the EPE and L_{syn} are of different units, we quantitatively assess the divergence between L_{syn} and EPE as their *monotonic* relationship, which is quantified using the Spearman’s Rank Coefficients r_s [28] due to its robustness against outliers and noise [31]. Given two sets of variables of size N that are co-observed, $X = \{x_i : i \in [1, N]\}$, $Y = \{y_i : i \in [1, N]\}$,

$$r_s = \frac{\frac{1}{N} \sum_{i=1}^N (R_{x_i} - \bar{R}_x) \cdot (R_{y_i} - \bar{R}_y)}{\sqrt{(\frac{1}{N} \sum_{i=1}^N R_{x_i} - \bar{R}_x) \cdot (\frac{1}{N} \sum_{i=1}^N R_{y_i} - \bar{R}_y)}} \quad (5)$$

where R is the rank and \bar{R} is the mean rank. In Equation 5, the numerator is the cross-covariance between R_X, R_Y while the denominator is the product of the covariances of R_X, R_Y . The coefficient r_s ranges from -1 to +1, with -1 indicating exact negative monotonic trend, +1 indicating exact positive monotonic trend, and 0 indicating no correlation as shown in Figure 2. Significance of r_s is reported via critical probability (p) values. We introduce the following definition of *divergence*:

Definition 1. Given two sets of variables of size N , $X = \{x_i : i \in [1, N]\}$, $Y = \{y_i : i \in [1, N]\}$, a divergence is observed between X, Y if both conditions are met

1. $r_s < 0.39$: where a weak or negative correlation between the two variables is observed,
2. $p < 0.05$: the result is statistically significant.

The above thresholds are adopted from the commonly established values [12, 29, 3]. We show in Appendix C that other thresholds used in different specialities do not affect the result significantly. Intuitively, divergence occurs when L_{syn} decreases while EPE 1) stagnates shown in Figure 2 (b), 2) decreases then increases (or vice versa) shown in Figure 2 (b), or 3) increases shown in Figure 2 (d).

2.6 Aleatoric Uncertainty

Uncertainty is an active topic in machine/deep learning. In general, uncertainty can be modeled as *epistemic* and *aleatoric* uncertainties [4]. Epistemic uncertainty refers to the ignorance of the model, for example, the limited capacity of a specific network architecture design. On the other hand, aleatoric uncertainty refers to the randomness of the problem or data itself. An example of aleatoric uncertainty is the coin flipping problem [15], where even if the best model is given, we still cannot obtain a definite head/tail prediction of next coin flip. We refer interested readers to [15] for in-depth

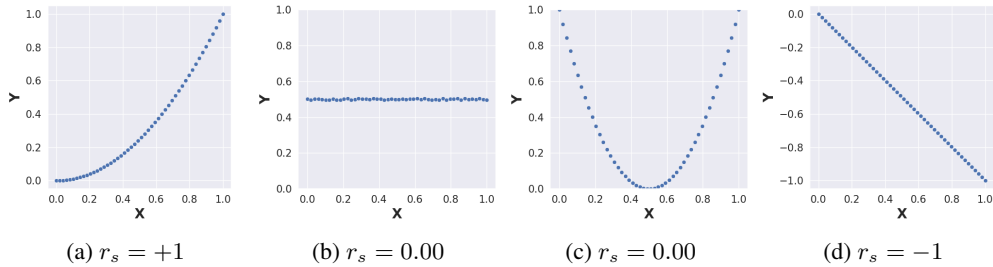


Figure 2: Examples of Spearman’s rank coefficients between two variables X, Y . (a) Positive, (b-c) weak and (d) negative monotonic relationship.

review of relevant literature. In this work, we try our best to reduce epistemic uncertainty by using various contemporary networks and ensure enough training of each network onto the target dataset, which leaves the observed divergence between image synthesis and depth estimation to aleatoric uncertainties originated from the training data.

In depth estimation literature, prior work such as [10, 22, 36] model aleatoric uncertainties with a pixel-wise mask to exclude certain pixels from the training process for better performance. The excluded pixels include occluded pixels that are not commonly observed by two frames and pixels of dynamic objects that break the static scene assumption. However, none of the prior work reported the diverging phenomenon even *after excluding* these pixels.

3 Experimental Setup

Instead of only reporting the final validation performance like prior work, we monitor how L_{syn} and EPE change respectively at each epoch to check if there is a divergence between L_{syn} and EPE.

3.1 Dataset

We conduct experiments on four datasets to demonstrate that the disagreement between L_{syn} and depth prediction error is not limited to a single domain. The datasets of interest provide varied image statistics and scene complexity. Furthermore, the ground truth data are captured with different depth modalities, which constitutes a stable backdrop for observing the effects of self-supervision. The datasets selected have corresponding ground truth depth, which can be used to monitor divergence. Since real datasets may have chromatic differences between left/right images, we align the left and right images appearance using a per-channel shift [17]. We normalize the images to 0-1 when computing L_{syn} to make SSIM valid [38]. More details about dataset used can be found in Appendix A.

3.1.1 Spatial Stereo Dataset

KITTI2015 [25] contains 200 pairs of images of street scenes of resolution 1242×375 with *sparse* ground truth disparity maps computed from LiDAR. We use the first 150 images for training and the rest 50 images for validation. SERV-CT [7] contains 16 pairs of *ex vivo* endoscopic images of resolution 720×576 with *dense* ground truth disparity maps computed from an aligned CT scan. We use the first 8 images for training and the remaining 8 images for validation. Middlebury2014 Q [30] contains 15 images of indoor scenes of various image resolution with *dense* disparity maps acquired via structured light. We use the first 10 images for training and the remaining 5 images for validation.

3.1.2 Temporal Stereo Dataset

Since dynamic objects violate the image synthesis assumption, we use the synthetic New Tsukuba Stereo Dataset fluorescent [23] which is static indoor scenes with associated ground truth camera pose and *dense* disparity maps. The resolution is 640×480 . We use the first 130 frames for training and the remaining 50 images for validation. Using this dataset allows us to investigate the temporal effect of self-supervised depth estimation.

3.2 Hyperparameters

We use the pre-trained weights provided by the authors (see Appendix A for more details). We scale the originally used learning rate by 0.1 as the pre-trained weights are well-initialized. We use the AdamW optimizer with a weight decay of $1e-4$ [21]. We demonstrate the choice of optimizer does not fundamentally change the result (see Appendix G).

We follow prior work [9, 35] and set $\alpha = 0.85$ in Equation 1, and set $C_1 = 1e-4$, $C_2 = 9e-4$, the kernel size used to compute μ, σ to 3×3 in Equation 2. We also show that these hyper-parameters (α and kernel size) marginally affect the result but do not resolve the divergence issue (see Appendix E and F). Following [10], we upsample disparities from each scale to full resolution and set weightings for L_{syn} from each scale to 1, and weighting for L_{smth} to $1e-2$. We train for 200 epochs on all dataset. We run all experiments on one Nvidia Titan RTX GPU.

4 Results and Discussion

4.1 Divergence in validation

The quantitative result is summarized in Table 1. Comparing the change of EPE from final to initial values, some networks are able to improve on certain dataset (highlighted as **blue**), which agrees with the conclusion of prior work that image synthesis improves the depth estimation. However, many networks have worse performance after optimizing for image-synthesis (highlighted as **red**). Furthermore, we note that the r_s is not always a positive number and often falls below the weak correlation threshold (highlighted as **red**), which indicates that EPE does not strictly follow the L_{syn} monotonically. The only strongly correlated case without any divergence is HSM trained on Middlebury2014. Fraction of divergence is also reported, where on average 0.54 of the data across different networks and dataset exhibit divergence.

We plot examples of divergence from two datasets in Figure 3. It is common to many networks that there exist a positive correlation between EPE and L_{syn} when L_{syn} is large, and after reaching the minima, the network worsens w.r.t depth afterwards. In other cases, the best operating point found is the starting point. This observation suggests a practical upper bound on depth estimation performance when optimizing for image synthesis: as a network improves on the target domain, further optimization of image synthesis can be harmful where networks fail to stabilize at the best optimal operating point found. Lastly, divergence is found in both spatial and temporal stereo dataset. We also observe divergence of L_{syn} and EPE when evaluated on the training data. Details can be found in Appendix B.

4.2 Change of EPE with decreasing L_{syn}

Instead of comparing the aggregated L_{syn} and EPE for the whole image, we instead compute the aggregated change of EPE only on pixels where L_{syn} is decreasing. This further isolates the inconsistent behavior. The quantitative result is summarized in Table 2. We note that even though in most cases the average ΔEPE is negative (*i.e.* a smaller error after training), the standard deviation is much larger, indicating many pixels have increasing error. We further highlight in red five cases where on average these pixels have increasing EPE. Therefore, minimization of L_{syn} is indeed not equivalent to minimization of EPE despite the theoretical justification of the image synthesis paradigm. Qualitative results can be found in Appendix D.

4.3 Ground Truth Disparity and Non-zero L_{syn}

In fact, we show that even with ground truth disparity, L_{syn} will not be 0 (Table 3). Therefore, if a network hypothetically predicts perfect disparity, non-zero gradients computed for L_{syn} w.r.t disparity will pass to the network. In this case, increasing L_{syn} may cause a larger perturbation of the model weights, leading to potentially divergent behavior. Though this non-zero gradient may be averaged out during the training process, we showed in Section 4.1 that divergence occurs after all. We visualize examples in Figure 4. Despite visual similarities between the actual and synthesized images, there are non-zero errors across the whole image. Appendix E provides additional experiment showing optimizing either L_{SSIM} and L_{L1} can lead to divergent learning.

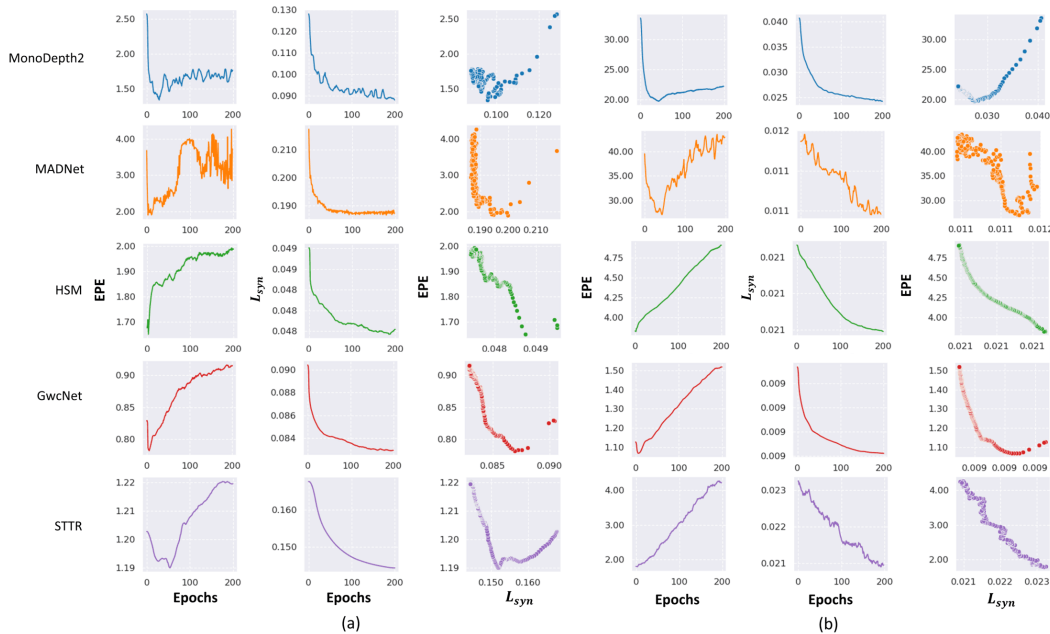


Figure 3: Validation result as training proceeds of (a) KITTI2015 dataset and (b) SERV-CT dataset.

Table 1: Validation result on four datasets. Δ : changes between final and initial EPE (**blue** indicates EPE decreases; **red** indicates EPE increases). r_s : Spearman’s Rank Coefficient (**blue** indicates average above 0.39; **red** indicates average below 0.39). Divergence: fraction of diverging training instances observed based on Definition 1.

| Dataset | Network | EPE | | | r_s | Divergence |
|----------------|------------|--------------|-------------|-----------------|-------------|------------|
| | | Initial | Final | Δ | | |
| KITTI2015 | MonoDepth2 | 6.24± 3.49 | 4.07± 2.72 | -2.18 (-35%) | +0.41± 0.38 | 0.20 |
| | MADNet | 8.28± 5.83 | 1.92± 1.70 | -6.35 (-73%) | +0.35± 0.45 | 0.36 |
| | HSM | 1.31± 0.42 | 1.27± 0.40 | -0.04 (-3%) | +0.04± 0.60 | 0.48 |
| | GwcNet | 1.27± 0.44 | 1.37± 0.47 | +0.10 (+9%) | -0.41± 0.58 | 0.82 |
| | STTR | 1.50± 0.81 | 2.53± 2.79 | +1.03 (+66%) | -0.01± 0.21 | 0.40 |
| SERV-CT | MonoDepth2 | 28.18± 5.31 | 11.85± 5.39 | -16.33 (-59%) | +0.65± 0.51 | 0.25 |
| | MADNet | 57.71± 23.67 | 35.10± 6.23 | -22.61 (-18%) | +0.34± 0.60 | 0.50 |
| | HSM | 2.38± 0.72 | 2.79± 1.00 | +0.42 (+18%) | -0.29± 0.67 | 0.62 |
| | GwcNet | 3.53± 1.89 | 2.73± 0.82 | -0.80 (-7%) | -0.58± 0.56 | 0.88 |
| | STTR | 3.70± 2.06 | 4.56± 3.05 | +0.86 (+20%) | -0.73± 0.38 | 1.00 |
| Middlebury2014 | MonoDepth2 | 17.07± 8.52 | 12.83± 8.58 | -4.24 (-28%) | -0.28± 0.83 | 0.60 |
| | MADNet | 13.06± 4.50 | 14.58± 3.88 | +1.52 (+18%) | -0.29± 0.51 | 0.60 |
| | HSM | 2.60± 1.57 | 2.10± 1.40 | -0.49 (-21%) | +0.89± 0.17 | 0.00 |
| | GwcNet | 3.07± 4.00 | 3.21± 4.17 | +0.14 (+4%) | +0.42± 0.60 | 0.20 |
| | STTR | 1.69± 2.66 | 1.33± 1.24 | -0.35 (-5%) | -0.58± 0.65 | 0.87 |
| Tsukuba | MonoDepth2 | 10.74± 4.09 | 8.45± 3.21 | -2.29 (-20%) | +0.26± 0.38 | 0.38 |
| | MADNet | 26.13± 11.99 | 16.57± 6.20 | -9.56 (-30%) | 0.00± 0.42 | 0.56 |
| | HSM | 1.66± 0.47 | 1.62± 0.39 | -0.04 (-1%) | +0.15± 0.47 | 0.48 |
| | GwcNet | 1.69± 1.14 | 1.79± 1.06 | +0.09 (+11%) | -0.68± 0.21 | 0.56 |
| | STTR | 2.01± 2.67 | 21.95± 7.98 | +19.94 (+1458%) | -0.89± 0.16 | 1.00 |
| Average | | | | | | 0.54 |

Table 2: Changes of EPE of pixels where L_{syn} decreases.

| Network | Δ EPE | | | |
|------------|--------------|---------------|----------------|-------------|
| | KITTI2015 | SERV-CT | Middlebury2014 | New Tsukuba |
| MonoDepth2 | -1.54± 3.98 | -24.20± 40.26 | -4.04± 11.77 | -0.54± 5.36 |
| MADNet | -1.95± 13.58 | -19.03± 27.36 | -0.60± 4.86 | +0.53± 3.35 |
| HSM | +1.30± 1.67 | +1.28± 4.97 | -0.66± 1.18 | -0.70± 3.88 |
| GwcNet | +0.25± 1.49 | -5.42± 19.26 | -0.12± 1.66 | -0.13± 1.75 |
| STTR | -1.06± 3.51 | -6.18± 20.14 | -0.13± 1.07 | +1.23± 4.11 |

Table 3: L_{syn} , L_{SSIM} and L_{L1} when ground truth disparity is used.

| | KITTI2015 | SERV-CT | Middlebury2014 | New Tsukuba |
|------------|-----------|---------|----------------|-------------|
| L_{syn} | 0.120 | 0.023 | 0.053 | 0.035 |
| L_{SSIM} | 0.132 | 0.023 | 0.057 | 0.039 |
| L_{L1} | 0.051 | 0.022 | 0.035 | 0.011 |

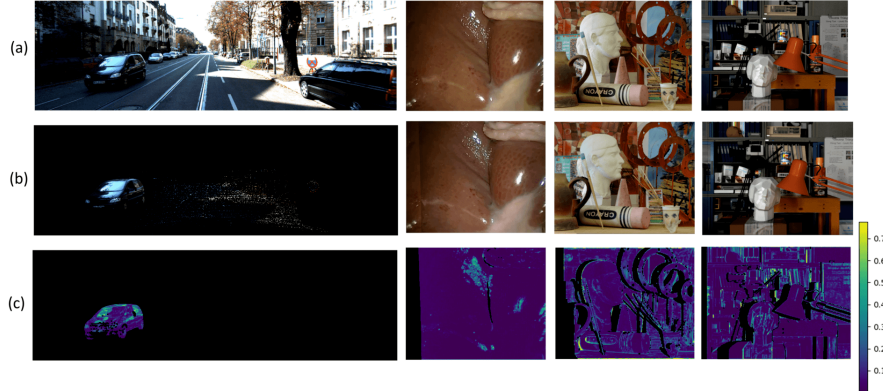


Figure 4: Visualization of (a) the input image, (b) the synthesized image, and (c) L_{syn} (occluded regions or regions without valid ground truth depth data are shown in black). Left to right: KITTI2015, SERV-CT, Middlebury2014 and New Tsukuba dataset.

4.4 Aleatoric Uncertainties of Image Synthesis

After observing the divergence, we analyze the loss landscapes [2] at places where divergence occurs in Figure 5. As shown, the optimization for image synthesis on a pixel level is non-convex w.r.t depth and deviates from the ground truth location (EPE= 0). We further elaborate below:

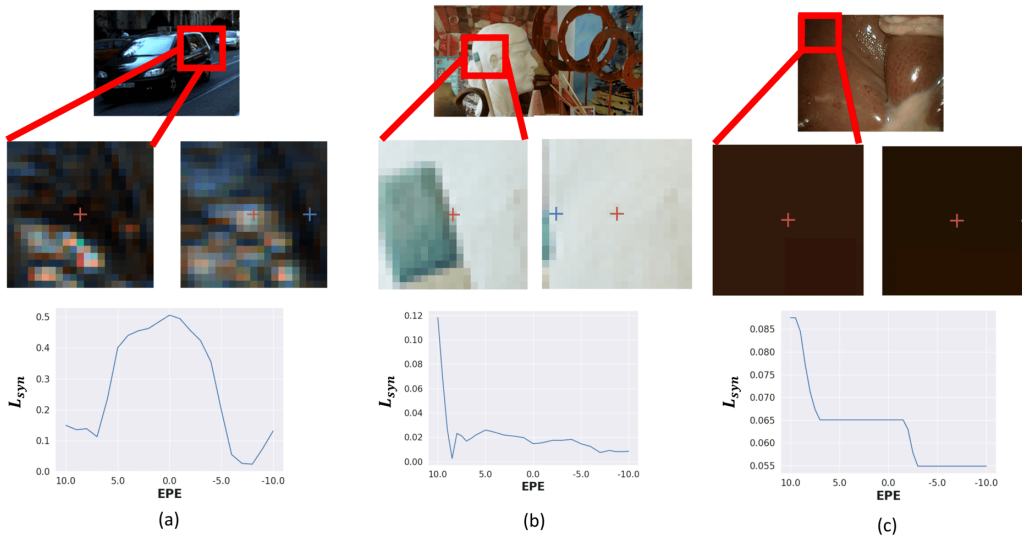


Figure 5: Aleatoric uncertainties and their associated loss landscapes. Top row: input images. Second row: zoom-in view of the primary image (left) and the neighboring image (right). Red cross indicates the corresponding pixels using ground truth depth and blue cross indicates the location of minimum L_{syn} found within the local window. Bottom row: loss landscape of L_{syn} w.r.t EPE.

Specular reflection and shadow - Specular reflection of non-Lambertian surfaces and shadow will occlude the true surface appearance and complicate the image synthesis process when it is observed at

different positions. One example is illustrated in Figure 5 (a) where differences between the reflection in the two images will conflate with the true disparity estimation value.

Object/occlusion edge - When a large disparity change occurs at object/occlusion edges, pixels will have different local context in primary and neighboring images, which will lead to false correspondences as shown in Figure 5 (b).

Lack of texture or repeated texture - At a textureless (over/under exposure or uniform texture) or repeated texture area, there are many possible values that can minimize L_{syn} , which makes image synthesis prone to error. Even if smoothness regularization is used, it does not guarantee the correctness of the disparity estimation (see video supplementary material).

5 Significance of the Finding

Our primary finding demonstrates that self-supervised optimization of L_{syn} is limited in its ability to improve depth prediction error, especially when depth estimation has improved to a sufficient extent during self-supervised learning. While there are cases where the final performance of depth estimation on a target domain may improve (which has been the focus of most published work to date), a network may, contrary to common belief, have divergent training and fail to stabilize at the best operating point found (Figure 3). This finding may point to inherent limitations of contemporary self-supervised methods for depth estimation, and further, cast doubt on the use of SSIM to compare the synthesized images against the primary image as an evaluation metric for assessing depth estimation performance without ground truth [14].

6 Conclusion and Limitations

In this work, we have empirically demonstrated a disagreement between the image synthesis loss and the final depth estimation accuracy during self-supervised learning of depth estimation. This phenomenon provides evidence for practical limits of image synthesis for decreasing depth prediction error due to aleatoric uncertainties. We found 127 papers use this paradigm, yet none of them reported such cases. While we cannot contribute a solution to this issue at the moment, we believe that this issue warrants discussion due to the growing prevalence of image synthesis-based self-supervision. Our results currently are limited to small datasets without large scale training due to the limited availability of ground truth data. Neither do we not consider the noise and artifacts associated with the ground truth data, which may influence the result. Future work may improve upon our findings by explicitly identifying the regions which exhibit aleatoric uncertainties. Exploring additional constraints beyond image synthesis (such as geometric information [39]) for training depth estimation networks and causal analysis [27] of the aleatoric uncertainties and divergence are of interest for future work.

References

- [1] Haldun Akoglu. User’s guide to correlation coefficients. *Turkish journal of emergency medicine*, 18(3):91–93, 2018.
- [2] Ran Cheng. Explore the Convexity of Photometric Loss. <https://rancheng.github.io/Explore-Convexity-Residual-Patterns/>. [Online; accessed 24-May-2021].
- [3] James E De Muth. *Basic statistics and pharmaceutical statistical applications*. CRC Press, 2014.
- [4] Armen Der Kiureghian and Ove Ditlevsen. Aleatory or epistemic? does it matter? *Structural safety*, 31(2):105–112, 2009.
- [5] Tom van Dijk and Guido de Croon. How do neural networks see depth in single images? In *Proceedings of the IEEE/CVF International Conference on Computer Vision*, pages 2183–2191, 2019.
- [6] John Duchi, Elad Hazan, and Yoram Singer. Adaptive subgradient methods for online learning and stochastic optimization. *Journal of machine learning research*, 12(7), 2011.

- [7] PJ Eddie’Edwards, Dimitris Psychogyios, Stefanie Speidel, Lena Maier-Hein, and Danail Stoyanov. Serv-ct: A disparity dataset from ct for validation of endoscopic 3d reconstruction. *arXiv e-prints*, pages arXiv–2012, 2020.
- [8] Andreas Geiger, Philip Lenz, Christoph Stiller, and Raquel Urtasun. Vision meets robotics: The kitti dataset. *The International Journal of Robotics Research*, 32(11):1231–1237, 2013.
- [9] Clément Godard, Oisin Mac Aodha, and Gabriel J Brostow. Unsupervised monocular depth estimation with left-right consistency. In *Proceedings of the IEEE Conference on Computer Vision and Pattern Recognition*, pages 270–279, 2017.
- [10] Clément Godard, Oisin Mac Aodha, Michael Firman, and Gabriel J Brostow. Digging into self-supervised monocular depth estimation. In *Proceedings of the IEEE/CVF International Conference on Computer Vision*, pages 3828–3838, 2019.
- [11] Alex Graves. Generating sequences with recurrent neural networks. *arXiv preprint arXiv:1308.0850*, 2013.
- [12] Joy Paul Guilford. *Fundamental statistics in psychology and education*. 1950.
- [13] Xiaoyang Guo, Kai Yang, Wukui Yang, Xiaogang Wang, and Hongsheng Li. Group-wise correlation stereo network. In *Proceedings of the IEEE/CVF Conference on Computer Vision and Pattern Recognition*, pages 3273–3282, 2019.
- [14] Shir Gur and Lior Wolf. Single image depth estimation trained via depth from defocus cues. In *Proceedings of the IEEE/CVF Conference on Computer Vision and Pattern Recognition*, pages 7683–7692, 2019.
- [15] Eyke Hüllermeier and Willem Waegeman. Aleatoric and epistemic uncertainty in machine learning: An introduction to concepts and methods. *Machine Learning*, 110(3):457–506, 2021.
- [16] Max Jaderberg, Karen Simonyan, Andrew Zisserman, and Koray Kavukcuoglu. Spatial transformer networks. *arXiv preprint arXiv:1506.02025*, 2015.
- [17] Hailin Jin, Paolo Favaro, and Stefano Soatto. Real-time feature tracking and outlier rejection with changes in illumination. In *Proceedings Eighth IEEE International Conference on Computer Vision. ICCV 2001*, volume 1, pages 684–689. IEEE, 2001.
- [18] Diederik P Kingma and Jimmy Ba. Adam: A method for stochastic optimization. *arXiv preprint arXiv:1412.6980*, 2014.
- [19] Ang Li and Zejian Yuan. Occlusion aware stereo matching via cooperative unsupervised learning. In *Asian Conference on Computer Vision*, pages 197–213. Springer, 2018.
- [20] Zhaoshuo Li, Xingtong Liu, Nathan Drenkow, Andy Ding, Francis X Creighton, Russell H Taylor, and Mathias Unberath. Revisiting stereo depth estimation from a sequence-to-sequence perspective with transformers. *arXiv preprint arXiv:2011.02910*, 2020.
- [21] Ilya Loshchilov and Frank Hutter. Decoupled weight decay regularization. *arXiv preprint arXiv:1711.05101*, 2017.
- [22] Chenxu Luo, Zhenheng Yang, Peng Wang, Yang Wang, Wei Xu, Ram Nevatia, and Alan Yuille. Every pixel counts++: Joint learning of geometry and motion with 3d holistic understanding. *IEEE transactions on pattern analysis and machine intelligence*, 42(10):2624–2641, 2019.
- [23] Sarah Martull, Martin Peris, and Kazuhiro Fukui. Realistic cg stereo image dataset with ground truth disparity maps. In *ICPR workshop TrakMark2012*, volume 111, pages 117–118, 2012.
- [24] Nikolaus Mayer, Eddy Ilg, Philip Hausser, Philipp Fischer, Daniel Cremers, Alexey Dosovitskiy, and Thomas Brox. A large dataset to train convolutional networks for disparity, optical flow, and scene flow estimation. In *Proceedings of the IEEE conference on computer vision and pattern recognition*, pages 4040–4048, 2016.
- [25] Moritz Menze and Andreas Geiger. Object scene flow for autonomous vehicles. In *Proceedings of the IEEE conference on computer vision and pattern recognition*, pages 3061–3070, 2015.

- [26] David Moher, Alessandro Liberati, Jennifer Tetzlaff, Douglas G Altman, Prisma Group, et al. Preferred reporting items for systematic reviews and meta-analyses: the prisma statement. *PLoS medicine*, 6(7):e1000097, 2009.
- [27] Judea Pearl. *Causality*. Cambridge university press, 2009.
- [28] Philip H Ramsey. Critical values for spearman’s rank order correlation. *Journal of educational statistics*, 14(3):245–253, 1989.
- [29] Derek Rowntree. *Statistics without tears: A primer for non-mathematicians*. Scribner Book Company, 1981.
- [30] Daniel Scharstein, Heiko Hirschmüller, York Kitajima, Greg Krathwohl, Nera Nešić, Xi Wang, and Porter Westling. High-resolution stereo datasets with subpixel-accurate ground truth. In *German conference on pattern recognition*, pages 31–42. Springer, 2014.
- [31] Patrick Schober, Christa Boer, and Lothar A Schwarte. Correlation coefficients: appropriate use and interpretation. *Anesthesia & Analgesia*, 126(5):1763–1768, 2018.
- [32] Alisha Sharma and Jonathan Ventura. Unsupervised learning of depth and ego-motion from cylindrical panoramic video. In *2019 IEEE International Conference on Artificial Intelligence and Virtual Reality (AIVR)*, pages 58–587. IEEE, 2019.
- [33] Ilya Sutskever, James Martens, George Dahl, and Geoffrey Hinton. On the importance of initialization and momentum in deep learning. In *International conference on machine learning*, pages 1139–1147. PMLR, 2013.
- [34] Richard Szeliski. *Computer vision: algorithms and applications*. Springer Science & Business Media, 2010.
- [35] Alessio Tonioni, Fabio Tosi, Matteo Poggi, Stefano Mattoccia, and Luigi Di Stefano. Real-time self-adaptive deep stereo. In *Proceedings of the IEEE/CVF Conference on Computer Vision and Pattern Recognition*, pages 195–204, 2019.
- [36] Sudheendra Vijayanarasimhan, Susanna Ricco, Cordelia Schmid, Rahul Sukthankar, and Katerina Fragkiadaki. Sfm-net: Learning of structure and motion from video. *arXiv preprint arXiv:1704.07804*, 2017.
- [37] Haiyang Wang, Xinchao Wang, Jie Song, Jie Lei, and Mingli Song. Faster self-adaptive deep stereo. In *Proceedings of the Asian Conference on Computer Vision*, 2020.
- [38] Zhou Wang, Alan C Bovik, Hamid R Sheikh, and Eero P Simoncelli. Image quality assessment: from error visibility to structural similarity. *IEEE transactions on image processing*, 13(4): 600–612, 2004.
- [39] Xingkui Wei, Yinda Zhang, Zhuwen Li, Yanwei Fu, and Xiangyang Xue. Deepsfm: Structure from motion via deep bundle adjustment. In *European conference on computer vision*, pages 230–247. Springer, 2020.
- [40] Junyuan Xie, Ross Girshick, and Ali Farhadi. Deep3d: Fully automatic 2d-to-3d video conversion with deep convolutional neural networks. In *European Conference on Computer Vision*, pages 842–857. Springer, 2016.
- [41] Gengshan Yang, Joshua Manela, Michael Happold, and Deva Ramanan. Hierarchical deep stereo matching on high-resolution images. In *Proceedings of the IEEE/CVF Conference on Computer Vision and Pattern Recognition*, pages 5515–5524, 2019.
- [42] Zhichao Yin and Jianping Shi. Geonet: Unsupervised learning of dense depth, optical flow and camera pose. In *Proceedings of the IEEE conference on computer vision and pattern recognition*, pages 1983–1992, 2018.
- [43] Hang Zhao, Orazio Gallo, Iuri Frosio, and Jan Kautz. Loss functions for neural networks for image processing. *arXiv preprint arXiv:1511.08861*, 2015.
- [44] Yiran Zhong, Hongdong Li, and Yuchao Dai. Open-world stereo video matching with deep rnn. In *Proceedings of the European Conference on Computer Vision (ECCV)*, pages 101–116, 2018.

Appendix

A Networks and Dataset Details

MonoDepth2 [10] is a SOTA monocular depth estimation network. The network predicts disparity through a sigmoid layer. The pre-trained weight used is named *stereo_640 × 192*, which is trained in a self-supervised setup using stereo images on KITTI RAW dataset [8] (which is different from KITTI 2015 dataset). The code and pre-trained weights are released under the *Monodepth v2 Liense*.

MADNet [35] is a stereo depth estimation network. The network has a correlation layer for predicting disparity. The pre-trained weight used is named *Sythetic*, which is trained with ground truth supervision using Scene Flow [24]. The code and pre-trained weights are released under the *Apache-2.0 License*.

HSM [23] is a stereo depth estimation network. The network uses 3D convolutions for predicting disparities. The pre-trained weight used is named *Middlebury model*, which is trained on customized datasets (see paper for more details). The code and pre-trained weights are released under the *MIT License*.

GwcNet [13] is a stereo depth estimation network. The network uses both correlation and 3D convolutions to predict disparities. The pre-trained weight used is provided in [20] which is trained using color-augmentation on Scene Flow [24] with ground truth supervision. The code and pre-trained weights are released under the *MIT License*.

STTR [20] is a stereo depth estimation network. The network is a transformer based network which uses attention to predict disparities. The pre-trained weight used is named *STTR-light*, which is trained using color-augmentation on Scene Flow [24]. The code and pre-trained weights are released under the *Apache-2.0 License*.

KITTI2015[25] uses the *CC BY-NC-SA 3.0 License*. SERV-CT [7] uses the *CC BY 4.0 License*. No license is provided for Middlebury2014 [30] and New Tsukuba [23] dataset. KITTI2015, SERV-CT and Middlebury2014 have distinct scenes for each data provided, while New Tsukuba provides a sequential observation of the same scene at 30 Hz. Due to the small camera motion for New Tsukuba, we downsample the frequency to 3 Hz.

B Divergence in Training

B.1 Divergence in Training

We also monitor L_{syn} and EPE for training data, where no generalization is required for the network. The quantitative result is shown in Table 4. The disagreement of L_{syn} and EPE is also evident on training data as the r_s rarely surpasses 0.39 and many networks have worse performance after self-supervised training. In fact, the average divergence cases of 0.61 is higher than 0.54 in the validation result (Table 1 in the manuscript), suggesting that over-optimizing for L_{syn} may harm the depth performance without any knowledge of the actual depth performance.

B.2 Effect of Regularization

Since we observe diverging phenomenon during refinement, we further ablate the training with different regularization setting to ensure that it is not caused by a specific regularization. We conduct four experiments for each network: baseline without any regularization, with smoothness regularization only (denoted as SMTH), with multi-scale regularization only (denoted as MS), and with both regularization. We have selected SERV-CT and Middlebury2014 dataset for this experiment since it has *dense* ground truth (allowing us to inspect every pixel) and distinct scene characteristics (medical and indoor). The quantitative result is summarized in Table 5.

We find that the commonly used regularization techniques do not always improve the final EPE performance. For example, for HSM/GwcNet/STTR trained on SERV-CT, the final EPE became worse than initial EPE after training (Δ column is **red**), regardless of the regularization techniques used. While it is commonly believed that using both regularizations gives the best result, we also find sometimes removing smoothness regularization leads to better result (MonoDepth2/MADNet/ trained

Table 4: Training result on four datasets. Δ : changes between final and initial EPE (**blue** indicates EPE decreases; **red** indicates EPE increases). r_s : Spearman’s Rank Coefficient (**blue** indicates average above 0.39; **red** indicates average below 0.39). Divergence: fraction of diverging training instances observed based on Definition 1.

| Dataset | Network | EPE | | | r_s | Divergence |
|----------------|------------|--------------|--------------|------------------------|--------------------|------------|
| | | Initial | Final | Δ | | |
| KITTI2015 | MonoDepth2 | 7.20± 3.08 | 1.46± 0.88 | -5.75 (-78%) | +0.54± 0.21 | 0.23 |
| | MADNet | 7.03± 12.18 | 1.74± 1.64 | -5.29 (-65%) | +0.38± 0.51 | 0.41 |
| | HSM | 1.21± 0.49 | 1.14± 0.66 | -0.07 (-7%) | +0.52± 0.58 | 0.29 |
| | GwcNet | 1.31± 2.08 | 1.32± 0.64 | +0.01 (+4%) | -0.67± 0.40 | 0.95 |
| | STTR | 1.46± 2.78 | 2.02± 3.29 | +0.56 (+37%) | -0.05± 0.24 | 0.99 |
| SERV-CT | MonoDepth2 | 35.62± 6.80 | 11.93± 5.45 | -23.69 (-67%) | +0.64± 0.49 | 0.25 |
| | MADNet | 36.03± 20.20 | 19.48± 10.62 | -16.55 (-32%) | -0.14± 0.59 | 0.88 |
| | HSM | 2.02± 0.72 | 3.03± 1.03 | +1.01 (+54%) | -1.00± 0.00 | 1.00 |
| | GwcNet | 2.22± 0.85 | 2.76± 0.80 | +0.54 (+32%) | -0.96± 0.05 | 1.00 |
| | STTR | 2.04± 0.76 | 4.21± 1.96 | +2.16 (+141%) | -0.18± 0.10 | 1.00 |
| Middlebury2014 | MonoDepth2 | 14.54± 4.11 | 10.95± 5.35 | -3.58 (-25%) | +0.48± 0.72 | 0.30 |
| | MADNet | 27.49± 13.09 | 17.54± 6.23 | -9.95 (-25%) | +0.16± 0.52 | 0.60 |
| | HSM | 2.05± 0.90 | 1.46± 0.66 | -0.59 (-26%) | +0.68± 0.55 | 0.20 |
| | GwcNet | 1.00± 0.37 | 0.83± 0.26 | -0.17 (-14%) | +0.19± 0.59 | 0.60 |
| | STTR | 1.66± 2.60 | 1.34± 1.24 | -0.33 (-5%) | -0.57± 0.65 | 0.87 |
| New Tsukuba | MonoDepth2 | 12.08± 6.65 | 3.84± 4.44 | -8.24 (-73%) | +0.85± 0.21 | 0.04 |
| | MADNet | 26.98± 11.62 | 17.37± 5.49 | -9.62 (-30%) | +0.36± 0.40 | 0.44 |
| | HSM | 1.74± 0.79 | 1.50± 0.51 | -0.24 (-10%) | +0.26± 0.59 | 0.48 |
| | GwcNet | 1.30± 0.46 | 1.40± 0.45 | +0.10 (+10%) | -0.72± 0.28 | 0.63 |
| | STTR | 1.39± 0.48 | 19.93± 10.42 | +18.54 (+1346%) | -0.94± 0.08 | 1.00 |
| Average | | | | | | 0.61 |

on SERV-CT and MonoDepth2/GwcNet trained on Middlebury2014) and sometimes removing multi-scale regularization leads to better result (HSM trained on SERV-CT). These findings suggest that regularization techniques do not fundamentally solve the divergence issue and can lead to inconsistent result depending on the network/dataset.

C Sensitivity Analysis of Thresholds for Definition 1

In Figure 6, we generate a set of simulation result where the original variables are perfectly correlated with $y = x^2$, with $x = \{0.0, 0.02, 0.04, \dots, 1.0\}$ at 0.02 interval. We add increasing corruption that is randomly sampled from the range $[0.0, \epsilon]$ to y to qualitatively illustrate the how Spearman’s Rank coefficient r_s changes as data change. As ϵ increased from 0.0 to 2.5, Spearman’s Rank Coefficient decreases from 1.0 to 0.29 and the correlation between x, y are becoming weaker.

One other well-established threshold of Spearman’s Rank coefficient r_s for weak correlation in the political and medical researches is 0.29 [1]. We present result in Table 1 again but recomputed with the new threshold. The presented results only differ in two cases (MADNet trained on KITTI2015 and Middlebury2014) and average divergence case changes from 0.54 to 0.50, thus indicating our definition of divergence in Definition 1 is not highly sensitive to the selected threshold.

D Change of EPE with decreasing L_{syn}

We provide qualitative results of the change of EPE with decreasing L_{syn} . We mask out the pixels that are occluded or with increasing L_{syn} as black color. As shown in Figure 7, while some of the pixels have decreasing EPE (cooler color), many have increased EPE (warmer color). The increasing EPE are particularly evident at occlusion/object edges, textureless areas and specular regions as discussed in Section 4.4.

E Effect of Weighting Between L_{SSIM} and L_{L1}

As discussed in Section 4.3, the gradient w.r.t disparity estimation will be non-zero due to the residual error (where gradient is loss times learning rate), this means if there is a network with perfect depth prediction, it will diverge from this point. We examine if weightings between L_{SSIM} and L_{L1} affect training behavior. We conduct three experiments, using the default weighting in Equation 1, using

Table 5: Training result on two datasets with different types of regularization. MS: multi-scale regularization. SMTH: smoothness regularization. Δ : changes between final and initial EPE (**blue** indicates EPE decreases; **red** indicates EPE increases). r_s : Spearman’s Rank Coefficient (**blue** indicates average above 0.39; **red** indicates average below 0.39). Divergence: fraction of diverging training instances observed based on Definition 1.

| Dataset | Network | Regularization | | EPE | | | r_s | Divergence |
|----------------|------------|----------------|------|---------------|---------------------|---------------|--------------|------------|
| | | MS | SMTH | initial | Final | Δ | | |
| SERV-CT | MonoDepth2 | | | 35.92 ± 9.93 | 16.86 ± 8.07 | -19.05 (-52%) | +0.59 ± 0.42 | 0.25 |
| | | | ✓ | | 17.02 ± 7.93 | -18.90 (-52%) | +0.54 ± 0.43 | 0.31 |
| | | ✓ | | | 16.81 ± 8.14 | -19.11 (-52%) | +0.53 ± 0.41 | 0.31 |
| | | ✓ | ✓ | | 17.00 ± 8.08 | -18.92 (-52%) | +0.47 ± 0.44 | 0.38 |
| | MADNet | | | 23.74 ± 9.68 | 8.07 ± 5.48 | -15.67 (-68%) | +0.65 ± 0.32 | 0.12 |
| | | | ✓ | | 8.06 ± 5.67 | -15.68 (-68%) | +0.69 ± 0.28 | 0.12 |
| | | ✓ | | | 8.05 ± 5.58 | -15.69 (-68%) | +0.66 ± 0.32 | 0.12 |
| | | ✓ | ✓ | | 7.97 ± 5.38 | -15.77 (-68%) | +0.60 ± 0.32 | 0.12 |
| | HSM | | | 2.13 ± 0.73 | 4.01 ± 2.29 | +1.88 (+93%) | -0.73 ± 0.48 | 0.88 |
| | | | ✓ | | 3.52 ± 1.99 | +1.39 (+68%) | -0.55 ± 0.61 | 0.88 |
| | | ✓ | | | 4.02 ± 2.53 | +1.89 (+92%) | -0.65 ± 0.45 | 0.94 |
| | | ✓ | ✓ | | 3.58 ± 2.17 | +1.44 (+70%) | -0.49 ± 0.58 | 0.75 |
| | GwcNet | | | 2.22 ± 0.85 | 5.33 ± 1.58 | +2.98 (+147%) | -0.99 ± 0.01 | 1.00 |
| | | | ✓ | | 3.10 ± 1.01 | +0.83 (+42%) | -0.96 ± 0.09 | 1.00 |
| | | ✓ | | | 5.41 ± 1.78 | +2.90 (+139%) | -1.00 ± 0.00 | 1.00 |
| | | ✓ | ✓ | | 2.76 ± 0.80 | +0.54 (+32%) | -0.96 ± 0.05 | 1.00 |
| | STTR | | | 3.44 ± 2.02 | 5.42 ± 3.50 | +1.98 (+57%) | -0.60 ± 0.60 | 0.81 |
| | | | ✓ | | 4.38 ± 2.81 | +0.93 (+29%) | -0.54 ± 0.58 | 0.88 |
| | | ✓ | | | 4.46 ± 2.66 | +1.02 (+32%) | -0.70 ± 0.36 | 0.94 |
| | | ✓ | ✓ | | 3.48 ± 1.83 | +0.03 (+5%) | -0.39 ± 0.53 | 0.81 |
| Middlebury2014 | MonoDepth2 | | | 14.54 ± 4.11 | 10.95 ± 5.41 | -3.75 (-26%) | +0.39 ± 0.87 | 0.30 |
| | | | ✓ | | 11.07 ± 5.16 | -3.58 (-25%) | +0.42 ± 0.83 | 0.30 |
| | | ✓ | | | 10.88 ± 5.37 | -3.70 (-26%) | +0.45 ± 0.76 | 0.30 |
| | | ✓ | ✓ | | 10.95 ± 5.35 | -3.58 (-25%) | +0.48 ± 0.72 | 0.30 |
| | MADNet | | | 27.49 ± 13.09 | 17.01 ± 6.07 | -11.01 (-29%) | +0.20 ± 0.56 | 0.40 |
| | | | ✓ | | 17.38 ± 6.09 | -10.44 (-26%) | +0.29 ± 0.51 | 0.30 |
| | | ✓ | | | 18.17 ± 6.20 | -9.14 (-25%) | +0.15 ± 0.52 | 0.30 |
| | | ✓ | ✓ | | 17.54 ± 6.23 | -9.95 (-25%) | +0.16 ± 0.52 | 0.40 |
| | HSM | | | 2.05 ± 0.90 | 1.24 ± 0.52 | -0.71 (-35%) | +0.20 ± 0.56 | 0.40 |
| | | | ✓ | | 1.30 ± 0.60 | -0.63 (-32%) | +0.29 ± 0.51 | 0.30 |
| | | ✓ | | | 1.24 ± 0.51 | -0.71 (-35%) | +0.15 ± 0.52 | 0.30 |
| | | ✓ | ✓ | | 1.27 ± 0.58 | -0.68 (-34%) | +0.16 ± 0.52 | 0.40 |
| | GwcNet | | | 1.00 ± 0.37 | 1.04 ± 0.94 | +0.09 (+6%) | +0.24 ± 0.65 | 0.40 |
| | | | ✓ | | 0.78 ± 0.21 | -0.17 (-14%) | -0.10 ± 0.74 | 0.50 |
| | | ✓ | | | 0.77 ± 0.24 | -0.23 (-19%) | -0.01 ± 0.67 | 0.50 |
| | | ✓ | ✓ | | 0.83 ± 0.26 | -0.17 (-14%) | +0.19 ± 0.59 | 0.60 |
| | STTR | | | 1.66 ± 2.60 | 2.34 ± 4.57 | +0.69 (+20%) | -0.74 ± 0.53 | 0.87 |
| | | | ✓ | | 2.48 ± 5.36 | +0.77 (+14%) | -0.64 ± 0.64 | 0.87 |
| | | ✓ | | | 2.05 ± 3.58 | +0.39 (+18%) | -0.63 ± 0.57 | 0.80 |
| | | ✓ | ✓ | | 1.34 ± 1.23 | -0.31 (-5%) | -0.57 ± 0.65 | 0.87 |

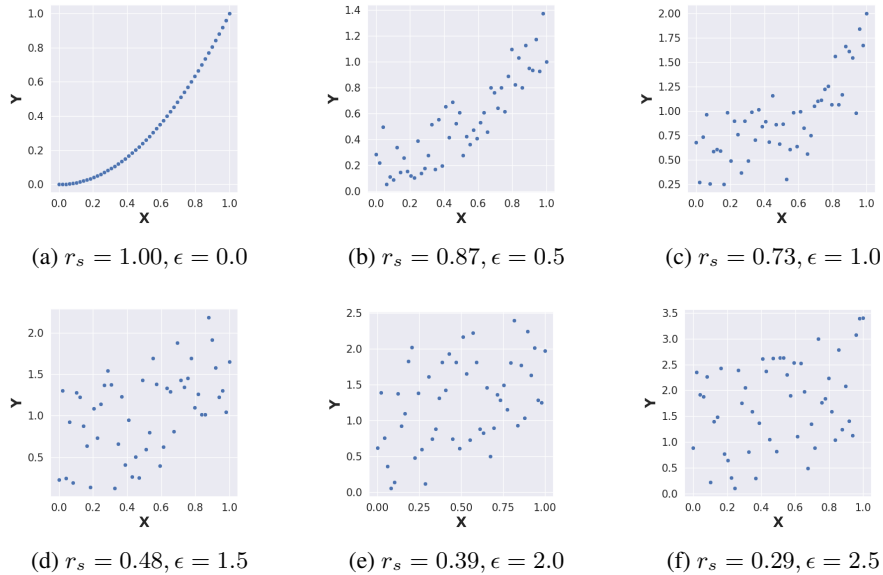


Figure 6: Simulation result of $y = x^2$ with increasing noise and decreasing Spearman’s Rank Coefficient r_s .

Table 6: Comparison of results with Spearman’s Rank coefficient r_s threshold being 0.39 and 0.29.

| Dataset | Network | Threshold=0.39 | | Threshold=0.29 | |
|----------------|------------|--------------------|------------|--------------------|------------|
| | | r_s | Divergence | r_s | Divergence |
| KITTI2015 | MonoDepth2 | +0.41± 0.38 | 0.20 | +0.41± 0.38 | 0.16 |
| | MADNet | +0.35± 0.45 | 0.36 | +0.35± 0.45 | 0.30 |
| | HSM | +0.04± 0.60 | 0.48 | +0.04± 0.60 | 0.44 |
| | GwcNet | -0.41± 0.58 | 0.82 | -0.41± 0.58 | 0.76 |
| | STTR | -0.01± 0.21 | 0.40 | -0.01± 0.21 | 0.38 |
| SERV-CT | MonoDepth2 | +0.65± 0.51 | 0.25 | +0.65± 0.51 | 0.25 |
| | MADNet | +0.34± 0.60 | 0.50 | +0.34± 0.60 | 0.25 |
| | HSM | -0.29± 0.67 | 0.62 | -0.29± 0.67 | 0.62 |
| | GwcNet | -0.58± 0.56 | 0.88 | -0.58± 0.56 | 0.88 |
| | STTR | -0.73± 0.38 | 1.00 | -0.73± 0.38 | 1.00 |
| Middlebury2014 | MonoDepth2 | -0.28± 0.83 | 0.60 | -0.28± 0.83 | 0.60 |
| | MADNet | -0.29± 0.51 | 0.60 | -0.29± 0.51 | 0.60 |
| | HSM | +0.89± 0.17 | 0.00 | +0.89± 0.17 | 0.00 |
| | GwcNet | +0.42± 0.60 | 0.20 | +0.42± 0.60 | 0.20 |
| | STTR | -0.58± 0.65 | 0.87 | -0.58± 0.65 | 0.87 |
| Tsukuba | MonoDepth2 | +0.26± 0.38 | 0.38 | +0.26± 0.38 | 0.22 |
| | MADNet | 0.00± 0.42 | 0.56 | 0.00± 0.42 | 0.48 |
| | HSM | +0.15± 0.47 | 0.48 | +0.15± 0.47 | 0.40 |
| | GwcNet | -0.68± 0.21 | 0.56 | -0.68± 0.21 | 0.52 |
| | STTR | -0.89± 0.16 | 1.00 | -0.89± 0.16 | 1.00 |
| Average | | | 0.54 | Average | 0.50 |

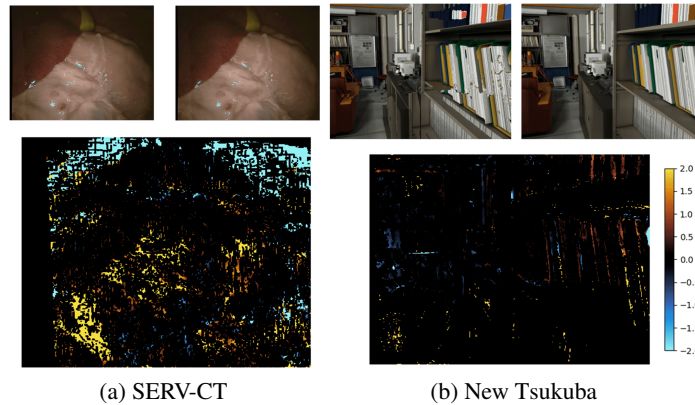


Figure 7: Visualization of synthesized images and change of EPE at places where L_{syn} decreases (black are either occluded regions or where L_{syn} increases). Top left figure is the initial synthesized image, top right figure is the final synthesized image, and the bottom figure is the change of EPE.

L_{SSIM} alone, and using L_{L1} alone. Experiments are conducted *with* multi-scale and smoothness regularization. Quantitative result is summarized in Table 7.

We find that there are cases where using either loss or a combination of them alone will lead to worse EPE, such as HSM/GwcNet trained on SERV-CT (Δ column is **red**). We conclude that the divergent problem is not due to the weighting of L_{SSIM} and L_{L1} , therefore adjusting the weight will not solve the divergence issue. We also find that using L_{L1} alone is consistently worse than using L_{SSIM} alone with the exception of MADNet trained on Middlebury2014, which justifies the larger weighting proposed for L_{SSIM} in [43, 9]. Moreover, we find that sometimes using L_{SSIM} alone is better, especially in dataset such as SERV-CT where many specular reflective regions are present.

F Effect of Kernel Size and Type in SSIM

As mentioned in Section 3.2, there can be variations of the L_{SSIM} . One parameter is the size of the local patch for computing μ, σ . The other parameter is the type of kernel used for computing μ, σ , one can use either linear kernels (where each pixels in the local patch are weighted equally) or Gaussian kernels. We conduct experiments to examine the effects of kernel size and kernel type for

Table 7: Training result on two datasets with different weightings between L_{SSIM} and L_{L1} . Δ : changes between final and initial EPE (**blue** indicates EPE decreases; **red** indicates EPE increases). r_s : Spearman’s Rank Coefficient (**blue** indicates average above 0.39; **red** indicates average below 0.39). Divergence: fraction of diverging training instances observed based on Definition 1.

| Dataset | Network | Weighting | | initial | EPE | | Δ | r_s | Divergence |
|---------|----------------|------------|----------|---------------|---------------------|----------------------|---------------------|--------------|------------|
| | | L_{SSIM} | L_{L1} | | Final | | | | |
| SERV-CT | MonoDepth2 | 1 | 0 | 35.92 ± 9.93 | 20.26 ± 9.47 | -15.65 (-44%) | +0.57 ± 0.43 | 0.25 | |
| | | 0 | 1 | | 21.02 ± 7.51 | -14.90 (-39%) | -0.07 ± 0.38 | 0.56 | |
| | | 0.85 | 0.15 | | 17.00 ± 8.08 | -18.92 (-52%) | +0.47 ± 0.44 | 0.38 | |
| | MADNet | 1 | 0 | 23.74 ± 9.68 | 7.97 ± 5.02 | -15.76 (-68%) | +0.67 ± 0.19 | 0.06 | |
| | | 0 | 1 | | 13.71 ± 6.11 | -10.03 (-40%) | +0.10 ± 0.34 | 0.56 | |
| | | 0.85 | 0.15 | | 7.97 ± 5.38 | -15.77 (-68%) | +0.60 ± 0.32 | 0.12 | |
| | HSM | 1 | 0 | 2.13 ± 0.73 | 2.96 ± 1.77 | +0.83 (+41%) | -0.22 ± 0.81 | 0.56 | |
| | | 0 | 1 | | 10.27 ± 5.46 | +8.14 (+420%) | -0.97 ± 0.05 | 1.00 | |
| | | 0.85 | 0.15 | | 3.58 ± 2.17 | +1.44 (+70%) | -0.49 ± 0.58 | 0.75 | |
| | GwcNet | 1 | 0 | 2.22 ± 0.85 | 2.26 ± 0.73 | +0.03 (+6%) | -0.86 ± 0.17 | 1.00 | |
| | | 0 | 1 | | 7.24 ± 2.57 | +4.97 (+251%) | -0.90 ± 0.18 | 1.00 | |
| | | 0.85 | 0.15 | | 2.76 ± 0.80 | +0.54 (+32%) | -0.96 ± 0.05 | 1.00 | |
| | STTR | 1 | 0 | 3.44 ± 2.02 | 3.20 ± 1.58 | -0.24 (-2%) | -0.26 ± 0.55 | 0.69 | |
| | | 0 | 1 | | 9.49 ± 5.36 | +6.05 (+197%) | -0.96 ± 0.07 | 1.00 | |
| | | 0.85 | 0.15 | | 3.48 ± 1.83 | +0.03 (+5%) | -0.39 ± 0.53 | 0.81 | |
| | Middlebury2014 | MonoDepth2 | 1 | 0 | 14.54 ± 4.11 | 11.24 ± 5.48 | -3.39 (-24%) | +0.41 ± 0.87 | 0.30 |
| | | | 0 | 1 | | 7.68 ± 2.83 | -6.15 (-43%) | +0.79 ± 0.53 | 0.10 |
| | | | 0.85 | 0.15 | | 10.95 ± 5.35 | -3.58 (-25%) | +0.48 ± 0.72 | 0.30 |
| MADNet | | 1 | 0 | 27.49 ± 13.09 | 17.26 ± 5.56 | -10.34 (-27%) | +0.16 ± 0.50 | 0.50 | |
| | | 0 | 1 | | 22.12 ± 10.10 | -5.55 (-13%) | -0.03 ± 0.52 | 0.40 | |
| | | 0.85 | 0.15 | | 17.54 ± 6.23 | -9.95 (-25%) | +0.16 ± 0.52 | 0.40 | |
| HSM | | 1 | 0 | 2.05 ± 0.90 | 1.28 ± 0.58 | -0.67 (-33%) | +0.83 ± 0.50 | 0.10 | |
| | | 0 | 1 | | 1.41 ± 0.60 | -0.54 (-27%) | +0.43 ± 0.61 | 0.30 | |
| | | 0.85 | 0.15 | | 1.27 ± 0.58 | -0.68 (-34%) | +0.16 ± 0.52 | 0.10 | |
| GwcNet | | 1 | 0 | 1.00 ± 0.37 | 0.84 ± 0.29 | -0.16 (-16%) | +0.57 ± 0.61 | 0.10 | |
| | | 0 | 1 | | 1.05 ± 0.38 | +0.05 (+5%) | -0.55 ± 0.52 | 0.80 | |
| | | 0.85 | 0.15 | | 0.83 ± 0.26 | -0.17 (-17%) | +0.19 ± 0.59 | 0.60 | |
| STTR | | 1 | 0 | 1.66 ± 2.60 | 1.69 ± 1.65 | +0.03 (+3%) | -0.61 ± 0.54 | 0.80 | |
| | | 0 | 1 | | 1.93 ± 1.33 | +0.27 (+37%) | -0.36 ± 0.72 | 0.90 | |
| | | 0.85 | 0.15 | | 1.34 ± 1.23 | -0.31 (-19%) | -0.57 ± 0.65 | 0.87 | |

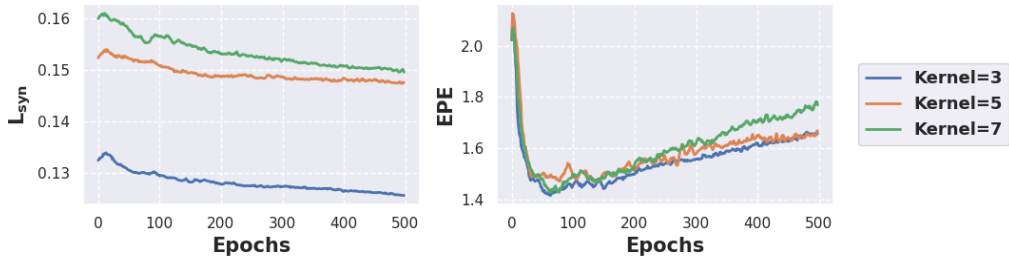
L_{syn} . We demonstrate that these parameters do not inherently change the training behavior as shown in Figure 8.

G Effect of Optimizer

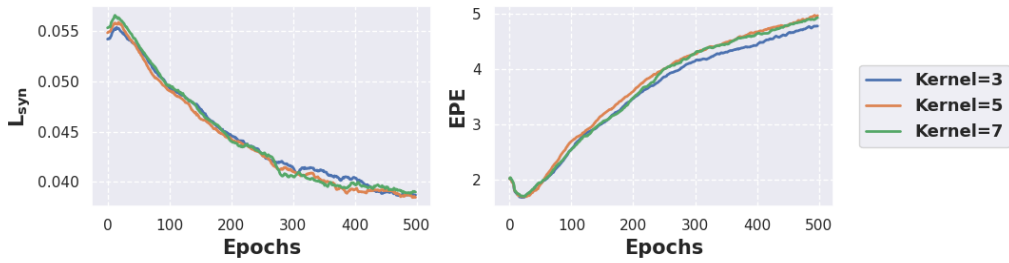
To eliminate the possibility that the specific choice of optimizer causes the disagreement, we conduct an ablation study for different optimizers using STTR, as STTR exhibits the worst divergence, including AdamW [21], Adam [18], Adagrad [6], RMSprop [11] and SGD with momentum [33]. All experiments are performed twice, with and without weight decay. The momentum is set to 0.9 where applicable. All experiments are performed with multi-scale and smoothness regularization. As shown in Figure 9, SGD suffers from gradient locality of L_{syn} , and does not make sufficient updates to the model. Adam, AdamW and RMSprop all lead to divergence between L_{syn} and depth prediction error after a certain point, especially RMSprop which minimizes L_{syn} the most. The only exception amongst the adaptive optimizers is Adagrad, which stops updating after a finite number of iterations due to gradient accumulation. This prevents L_{syn} from decreasing and thus avoids the inconsistency between L_{syn} and EPE, which can be a temporary alternative. However, because there is no good control over when the gradient magnitude will diminish with Adagrad, we feel that it is inadequate in practice.

H Synthesis Loss Beyond Intensities

An alternative to using image intensities for L_{syn} would be to use features extracted by the network. However, if a network already has the ability to distinguish each pixel and match them properly, the network should already predict the perfect disparity. Furthermore, we hypothesize that this learning paradigm introduces instability as the network can freely alter the feature representation compared to computing L_{syn} on image intensities. Regardless, we conduct a single experiment using features extracted by the network to compute L_{syn} to verify the hypothesis. The experiment is conducted on STTR with both multi-scale and smoothness regularization. As shown in Figure 10, due to a lack of constraints, the EPE increases much more faster compared to computing L_{syn} using image intensities.



(a) Linear Kernel (pixels are equally weighted)



(b) Gaussian Kernel

Figure 8: Comparison of kernel size and kernel type for L_{SSIM} computation.

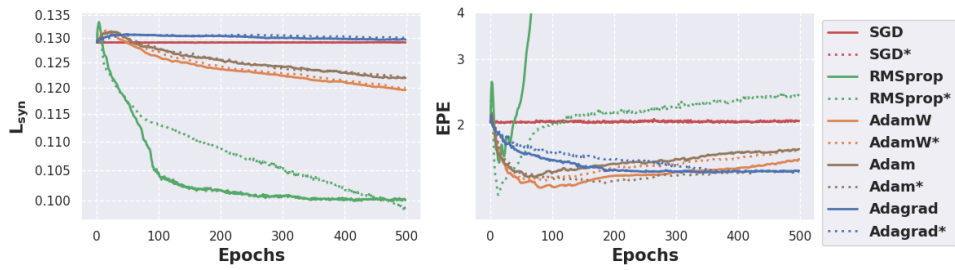


Figure 9: Ablation of different optimizers. Asterisk indicates presence of weight decay.

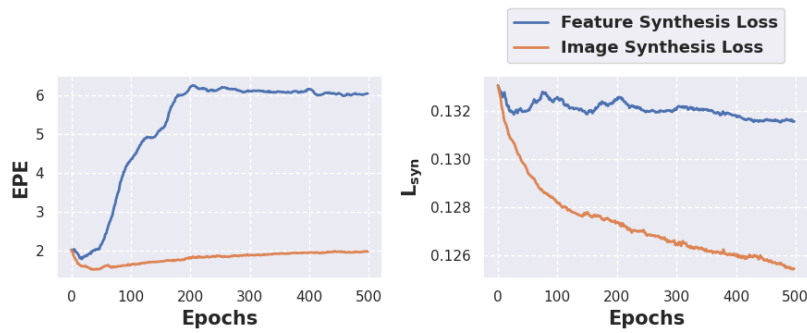


Figure 10: Ablation of L_{syn} on features and image intensities.

I Survey of Papers Using Image synthesis Loss

Following PRISMA guidelines [26], we conducted a literature review on self-supervised depth estimation using L_{syn} . Since the primary objective of this review is to estimate the scope of image synthesis-based self-supervision, we surveyed the arXiv database with the following search keywords:

- For monocular depth estimation - (self-supervised \vee unsupervised) \wedge (depth \vee disparity) \wedge (estimation \vee prediction);
- For stereo depth estimation - (self-supervised \vee unsupervised \vee adapt) \wedge (depth \vee disparity) \wedge (stereo).

This search retrieved a total of 447 papers that were then screened further based on the following inclusion criteria:

- Must be monocular or stereo depth estimation from images;
- Must use L_{syn} loss or other combination of L_{SSIM} and L_{L1} ;
- Must be original primary investigation (i.e. not a review paper);
- Language must be English;
- Published 2015 and up to June 1st, 2021.

After screening, 190 papers were included for full text review. A total of 63 papers were subsequently rejected after full text review, leaving 127 papers that fit the inclusion criteria. Among the selected papers, 114 papers use smoothness regularization, 67 papers use multi-scale regularization and 69 papers handle occlusion explicitly.

Table 8: Summary of literature review on self-supervised depth estimation using image synthesis. M/S: Depth from monocular or stereo images. SMTH: Smoothness regularization. MS: Multi-scale regularization. Occlusion: Occlusion handling.

| Paper ID | Title | Author Name | Year | M/S | SMTH | MS | Occlusion |
|----------|---|-------------|------|------|------|----|-----------|
| 1 | Improved Point Transformation Methods For Self-Supervised Depth Prediction | Ziwen | 2021 | S | x | x | ✓ |
| 2 | Learning Depth via Leveraging Semantics: Self-supervised Monocular Depth Estimation with Both Implicit and Explicit Semantic Guidance | Li | 2021 | M | ✓ | ✓ | x |
| 3 | Learning Monocular Depth in Dynamic Scenes via Instance-Aware Projection Consistency | Lee | 2021 | M | ✓ | ✓ | x |
| 4 | Self-supervised monocular depth estimation from oblique UAV videos | Maadhuanand | 2020 | M | ✓ | x | ✓ |
| 5 | Semantic-Guided Representation Enhancement for Self-supervised Monocular Trained Depth Estimation | Li | 2020 | M | ✓ | ✓ | x |
| 6 | HR-Depth : High Resolution Self-Supervised Monocular Depth Estimation | Lyu | 2020 | M | ✓ | ✓ | ✓ |
| 7 | Variational Monocular Depth Estimation for Reliability Prediction | Hirose | 2020 | M | ✓ | x | x |
| 8 | Attentional Separation-and-Aggregation Network for Self-supervised Depth-Pose Learning in Dynamic Scenes | Gao | 2020 | M | ✓ | x | ✓ |
| 9 | Unsupervised Monocular Depth Learning with Integrated Intrinsic and Spatio-Temporal Constraints | Chen | 2020 | M | ✓ | x | x |
| 10 | Unsupervised Deep Persistent Monocular Visual Odometry and Depth Estimation in Extreme Environments | Almaloglu | 2020 | M | ✓ | x | ✓ |
| 11 | Unsupervised Monocular Depth Learning in Dynamic Scenes | Li | 2020 | M | ✓ | x | ✓ |
| 12 | Geometry-based Occlusion-Aware Unsupervised Stereo Matching for Autonomous Driving | Peng | 2020 | S | ✓ | x | ✓ |
| 13 | Unsupervised Learning of Depth and Ego-Motion from Cylindrical Panoramic Video with Applications for Virtual Reality | Sharma | 2020 | M | ✓ | ✓ | x |
| 14 | SAFE-Net: Self-Supervised Monocular Depth Estimation with Semantic-Aware Feature Extraction | Choi | 2020 | M | ✓ | x | x |
| 15 | Calibrating Self-supervised Monocular Depth Estimation | McCrath | 2020 | M | ✓ | x | x |
| 16 | Cascade Network for Self-Supervised Monocular Depth Estimation | Chai | 2020 | M | ✓ | ✓ | x |
| 17 | Self-Supervised Learning for Monocular Depth Estimation from Aerial Imagery | Hermann | 2020 | M | ✓ | ✓ | ✓ |
| 18 | Reversing the cycle: self-supervised deep stereo through enhanced monocular distillation | Aleotti | 2020 | S | ✓ | ✓ | ✓ |
| 19 | Neural Ray Surfaces for Self-Supervised Learning of Depth and Ego-motion | Vasiljevic | 2020 | M | ✓ | x | x |
| 20 | SynDistNet: Self-Supervised Monocular Fisheye Camera Distance Estimation Synergized with Semantic Segmentation for Autonomous Driving | Kumar | 2020 | M | ✓ | x | ✓ |
| 21 | S3Net: Semantic-Aware Self-supervised Depth Estimation with Monocular Videos and Synthetic Data | Cheng | 2020 | M | ✓ | x | x |
| 22 | P2Net: Patch-match and Plane-regularization for Unsupervised Indoor Depth Estimation | Yu | 2020 | M | ✓ | x | x |
| 23 | P2D: a self-supervised method for depth estimation from polarimetry | Blanchon | 2020 | M | ✓ | x | ✓ |
| 24 | Self-Supervised Monocular Depth Estimation: Solving the Dynamic Object Problem by Semantic Guidance | Klingner | 2020 | M | ✓ | ✓ | x |
| 25 | UnRectDepthNet: Self-Supervised Monocular Depth Estimation using a Generic Framework for Handling Common Camera Distortion Models | Kumar | 2020 | M | ✓ | ✓ | ✓ |
| 26 | Continual Adaptation for Deep Stereo | Poggii | 2020 | S | ✓ | ✓ | x |
| 27 | Self-supervised Depth Estimation to Regularise Semantic Segmentation in Knee Arthroscopy | Liu | 2020 | M | x | ✓ | x |
| 28 | EndoSLAM Dataset and An Unsupervised Monocular Visual Odometry and Depth Estimation Approach for Endoscopic Videos: Endo-SFMLearner | Ozyoruk | 2020 | M | ✓ | x | x |
| 29 | MiniNet: An extremely lightweight convolutional neural network for real-time unsupervised monocular depth estimation | Liu | 2020 | | ✓ | ✓ | ✓ |
| 30 | Increased-Range Unsupervised Monocular Depth Estimation | Imran | 2020 | M | ✓ | ✓ | ✓ |
| 31 | Consistency Guided Scene Flow Estimation | Chen | 2020 | S | ✓ | x | ✓ |
| 32 | Self-Supervised Joint Learning Framework of Depth Estimation via Implicit Cues | Wang | 2020 | M, S | ✓ | ✓ | ✓ |
| 33 | Semantics-Driven Unsupervised Learning for Monocular Depth and Ego-Motion Estimation | Wei | 2020 | M | ✓ | x | ✓ |

| | | | | | | | | |
|----|---|------------|------|------|---|---|---|---|
| 34 | Unsupervised Depth Learning in Challenging Indoor Video: Weak Rectification to Rescue | Biang | 2020 | M | ✓ | ✓ | x | ✓ |
| 35 | Self-Attention Dense Depth Estimation Network for Unrectified Video Sequences | Mathew | 2020 | M | ✓ | ✓ | x | x |
| 36 | Deep feature fusion for self-supervised monocular depth prediction | Kaushik | 2020 | M | ✓ | ✓ | ✓ | ✓ |
| 37 | Self-Supervised Human Depth Estimation from Monocular Videos | Tan | 2020 | M | ✓ | ✓ | x | ✓ |
| 38 | Self-Supervised Attention Learning for Depth and Ego-motion Estimation | Sadek | 2020 | M | ✓ | ✓ | x | ✓ |
| 39 | Pseudo RGB-D for Self-Improving Monocular SLAM and Depth Prediction | Triwari | 2020 | M | ✓ | ✓ | x | x |
| 40 | RealMonoDepth: Self-Supervised Monocular Depth Estimation for General Scenes | Ocal | 2020 | M | ✓ | ✓ | ✓ | ✓ |
| 41 | Masked GANs for Unsupervised Depth and Pose Prediction with Scale Consistency | Zhao | 2020 | M | ✓ | ✓ | x | ✓ |
| 42 | Self-Supervised Monocular Scene Flow Estimation | Hur | 2020 | M | ✓ | ✓ | x | ✓ |
| 43 | Distilled Semantics for Comprehensive Scene Understanding from Videos | Tosi | 2020 | M | ✓ | ✓ | x | ✓ |
| 44 | Self-supervised Monocular Trained Depth Estimation using Self-attention and Discrete Disparity Volume | Johnston | 2020 | M | ✓ | ✓ | ✓ | ✓ |
| 45 | Defeat-Net: General Monocular Depth via Simultaneous Unsupervised Representation Learning | Spencer | 2020 | M | ✓ | ✓ | x | ✓ |
| 46 | DiPE: Deeper into Photometric Errors for Unsupervised Learning of Depth and Ego-motion from Monocular Videos | Jiang | 2020 | M | ✓ | ✓ | ✓ | ✓ |
| 47 | Unsupervised Learning of Depth, Optical Flow and Pose with Occlusion from 3D Geometry | Wang | 2020 | M | ✓ | ✓ | x | ✓ |
| 48 | Semantically-Guided Representation Learning for Self-Supervised Monocular Depth | Guizilimi | 2020 | M | ✓ | ✓ | ✓ | ✓ |
| 49 | Single Image Depth Estimation Trained via Depth from Defocus Cues | Gur | 2020 | M | ✓ | ✓ | x | x |
| 50 | Don't Forget The Past: Recurrent Depth Estimation from Monocular Video | Patil | 2020 | M | ✓ | ✓ | ✓ | ✓ |
| 51 | Self-supervised Object Motion and Depth Estimation from Video | Dai | 2020 | M | ✓ | ✓ | ✓ | x |
| 52 | Edge-Guided Occlusion Fading Reduction for a Light-Weighted Self-Supervised Monocular Depth Estimation | Peng | 2019 | M | ✓ | ✓ | x | ✓ |
| 53 | Unsupervised Monocular Depth Prediction for Indoor Continuous Video Streams | Feng | 2019 | M | ✓ | ✓ | ✓ | ✓ |
| 54 | Unsupervised High-Resolution Depth Learning From Videos With Dual Networks | Zhou | 2019 | M | ✓ | ✓ | ✓ | ✓ |
| 55 | FisheyeDistanceNet: Self-Supervised Scale-Aware Distance Estimation using Monocular Fisheye Camera for Autonomous Driving | Kumar | 2020 | M | ✓ | ✓ | x | ✓ |
| 56 | Self-Supervised Learning of Depth and Ego-motion with Differentiable Bundle Adjustment | Shi | 2019 | M | ✓ | ✓ | ✓ | x |
| 57 | Spherical View Synthesis for Self-Supervised 360° Depth Estimation | Ziculis | 2019 | M | ✓ | ✓ | x | x |
| 58 | Progressive Fusion for Unsupervised Binocular Depth Estimation using Cycled Networks | Pflzer | 2019 | S | x | ✓ | ✓ | x |
| 59 | Learning Residual Flow as Dynamic Motion from Stereo Videos | Lee | 2019 | S | ✓ | ✓ | ✓ | ✓ |
| 60 | Unsupervised Domain Adaptation for Depth Prediction from Images | Tonioni | 2019 | M | ✓ | ✓ | x | ✓ |
| 61 | MVS2: Deep Unsupervised Multi-view Stereo with Multi-View Symmetry | Dai | 2019 | S | ✓ | ✓ | x | ✓ |
| 62 | Improving Self-Supervised Single View Depth Estimation by Masking Occlusion | Schellevis | 2019 | M | ✓ | ✓ | ✓ | ✓ |
| 63 | Unsupervised Scale-consistent Depth and Ego-motion Learning from Monocular Video | Bian | 2019 | M | ✓ | ✓ | x | ✓ |
| 64 | Self-Supervised Learning With Geometric Constraints in Monocular Video: Connecting Flow, Depth, and Camera | Chen | 2019 | M | ✓ | ✓ | ✓ | x |
| 65 | Non-destructive three-dimensional measurement of hand vein based on self-supervised network | Chen | 2019 | S | ✓ | ✓ | x | x |
| 66 | Bridging Stereo Matching and Optical Flow via Spatiotemporal Correspondence | Lai | 2019 | S | ✓ | ✓ | ✓ | ✓ |
| 67 | Unsupervised Depth Completion from Visual Inertial Odometry | Wong | 2020 | M | ✓ | ✓ | x | x |
| 68 | Semi-Supervised Monocular Depth Estimation with Left-Right Consistency Using Deep Neural Network | Amiri | 2019 | M | ✓ | ✓ | ✓ | x |
| 69 | Learning Unsupervised Multi-View Stereopsis via Robust Photometric Consistency | Khot | 2019 | S | ✓ | ✓ | x | ✓ |
| 70 | 3D Packing for Self-Supervised Monocular Depth Estimation | Guizilimi | 2020 | M | ✓ | ✓ | ✓ | ✓ |
| 71 | Learn Stereo, Infer Mono: Siamese Networks for Self-Supervised, Monocular, Depth Estimation | Goldman | 2019 | M, S | ✓ | ✓ | ✓ | ✓ |
| 72 | Recurrent Neural Network for (Un-)supervised Learning of Monocular Video Visual Odometry and Depth | Wang | 2019 | M | ✓ | ✓ | ✓ | ✓ |

| | | | | | | | | |
|-----|---|-------------|------|------|---|---|---|---|
| 73 | Learning monocular depth estimation infusing traditional stereo knowledge | Tosi | 2019 | M | ✓ | ✓ | ✓ | ✓ |
| 74 | Learning to Adapt for Stereo | Tiononi | 2019 | S | x | x | x | ✓ |
| 75 | Geometry-Aware Symmetric Domain Adaptation for Monocular Depth Estimation | Zhao | 2019 | M | ✓ | x | x | x |
| 76 | A Novel Monocular Disparity Estimation Network with Domain Transformation and Ambiguity Learning | Bello | 2019 | M | ✓ | ✓ | ✓ | ✓ |
| 77 | Refine and Distill: Exploiting Cycle-Inconsistency and Knowledge Distillation for Unsupervised Monocular Depth Estimation | Plizer | 2019 | M | x | ✓ | ✓ | x |
| 78 | Unsupervised Cross-spectral Stereo Matching by Learning to Synthesize | Liang | 2019 | S | ✓ | ✓ | ✓ | x |
| 79 | Region Deformer Networks for Unsupervised Depth Estimation from Unconstrained Monocular Videos | Xu | 2019 | M | ✓ | ✓ | ✓ | ✓ |
| 80 | Unsupervised monocular stereo matching | Zhang | 2018 | M | ✓ | ✓ | ✓ | x |
| 81 | Unsupervised Learning of Monocular Depth Estimation with Bundle Adjustment, Super-Resolution and Clip Loss | Zhou | 2018 | M | ✓ | ✓ | ✓ | ✓ |
| 82 | Joint Unsupervised Learning of Optical Flow and Depth by Watching Stereo Videos | Wang | 2018 | S | ✓ | ✓ | x | ✓ |
| 83 | SuperDepth: Self-Supervised, Super-Resolved Monocular Depth Estimation | Pillai | 2018 | M | ✓ | ✓ | ✓ | ✓ |
| 84 | DispSegNet: Leveraging Semantics for End-to-End Learning of Disparity Estimation from Stereo Imagery | Zhang | 2019 | S | ✓ | ✓ | x | ✓ |
| 85 | Learning structure-from-motion from motion | Pinard | 2018 | M | ✓ | ✓ | ✓ | ✓ |
| 86 | DF-Net: Unsupervised Joint Learning of Depth and Flow using Cross-Task Consistency | Zhou | 2018 | M | ✓ | ✓ | ✓ | ✓ |
| 87 | A Deeper Insight into the UNDEMoN: Unsupervised Deep Network for Depth and Ego-Motion Estimation | Babu V | 2018 | M | ✓ | ✓ | ✓ | x |
| 88 | Learning monocular depth by distilling cross-domain stereo networks | Guo | 2018 | M | ✓ | ✓ | ✓ | ✓ |
| 89 | Learning monocular depth estimation with unsupervised trinocular assumptions | Poggii | 2018 | M | ✓ | ✓ | ✓ | ✓ |
| 90 | Towards real-time unsupervised monocular depth estimation on CPU | Poggii | 2018 | M | ✓ | ✓ | ✓ | x |
| 91 | Every Pixel Counts: Unsupervised Geometry Learning with Holistic 3D Motion Understanding | Yang | 2018 | M | ✓ | ✓ | ✓ | ✓ |
| 92 | Digging Into Self-Supervised Monocular Depth Estimation | Godard | 2019 | M | ✓ | ✓ | ✓ | ✓ |
| 93 | Competitive Collaboration: Joint Unsupervised Learning of Depth, Camera Motion, Optical Flow and Motion Segmentation | Ranjan | 2019 | M | ✓ | ✓ | ✓ | ✓ |
| 94 | Position Estimation of Camera Based on Unsupervised Learning | Wu | 2018 | M | x | x | x | x |
| 95 | Dual CNN Models for Unsupervised Monocular Depth Estimation | Repala | 2019 | M | ✓ | ✓ | ✓ | x |
| 96 | On the importance of Stereo for Accurate Depth Estimation: An Efficient Semi-Supervised Deep Neural Network Approach | Smolyanskiy | 2020 | S | ✓ | x | x | x |
| 97 | Fusion of stereo and still monocular depth estimates in a self-supervised learning context | Martins | 2018 | M, S | x | x | x | x |
| 98 | LEGO: Learning Edge with Geometry all at Once by Watching Videos | Yang | 2018 | M | ✓ | ✓ | ✓ | x |
| 99 | Self-Supervised Monocular Image Depth Learning and Confidence Estimation | Chen | 2018 | M | ✓ | ✓ | ✓ | x |
| 100 | Unsupervised Learning of Monocular Depth Estimation and Visual Odometry with Deep Feature Reconstruction | Zhan | 2018 | S | ✓ | ✓ | x | x |
| 101 | Geonet: Unsupervised learning of dense depth, optical flow and camera pose | Yin | 2018 | M | ✓ | ✓ | ✓ | ✓ |
| 102 | AdaDepth: Unsupervised Content Congruent Adaptation for Depth Estimation | Kundu | 2018 | M | x | x | x | x |
| 103 | Unsupervised Odometry and Depth Learning for Endoscopic Capsule Robots | Turan | 2018 | M | ✓ | ✓ | ✓ | ✓ |
| 104 | Unsupervised Learning of Depth and Ego-Motion from Monocular Video Using 3D Geometric Constraints | Mahjourian | 2018 | M | ✓ | ✓ | ✓ | x |
| 105 | Learning Depth from Monocular Videos using Direct Methods | Wang | 2017 | M | ✓ | ✓ | ✓ | x |
| 106 | Unsupervised Learning of Geometry with Edge-aware Depth-Normal Consistency | Yang | 2017 | M | x | ✓ | ✓ | x |
| 107 | UnDeepVO: Monocular Visual Odometry through Unsupervised Deep Learning | Li | 2018 | M | x | x | x | x |
| 108 | Multi-task Self-Supervised Visual Learning | Doersch | 2017 | M | x | x | x | x |

| | | | | | | | | | |
|-----|---|------------------|--|------|---|--|---|---|---|
| 109 | Self-Supervised Siamese Learning on Stereo Image Pairs for Depth Estimation in Robotic Surgery | Ye | | 2017 | S | | x | x | x |
| 110 | Unsupervised Learning of Depth and Ego-Motion from Video | Zhou | | 2017 | M | | ✓ | ✓ | x |
| 111 | SfM-Net: Learning of Structure and Motion from Video | Vijayanarasimhan | | 2017 | M | | ✓ | x | x |
| 112 | Unsupervised monocular depth estimation with left-right consistency | Godard | | 2017 | M | | ✓ | ✓ | ✓ |
| 113 | Unsupervised CNN for Single View Depth Estimation: Geometry to the Rescue | Garg | | 2016 | S | | ✓ | ✓ | x |
| 114 | EffiScene: Efficient Per-Pixel Rigidity Inference for Unsupervised Joint Learning of Optical Flow, Depth, Camera Pose and Motion Segmentation | Jiao | | 2020 | S | | ✓ | x | ✓ |
| 115 | Parallax Attention for Unsupervised Stereo Correspondence Learning | Wang | | 2020 | S | | ✓ | ✓ | ✓ |
| 116 | Self-Supervised Scale Recovery for Monocular Depth and Egomotion Estimation | Wagstaff | | 2020 | M | | ✓ | x | x |
| 117 | Monocular Depth Estimation with Self-supervised Instance Adaptation | McCraith | | 2020 | M | | ✓ | x | ✓ |
| 118 | Toward Hierarchical Self-Supervised Monocular Absolute Depth Estimation for Autonomous Driving Applications | Xue | | 2020 | M | | ✓ | ✓ | x |
| 119 | AdaStereo: A Simple and Efficient Approach for Adaptive Stereo Matching | Song | | 2020 | S | | ✓ | x | ✓ |
| 120 | Enhancing self-supervised monocular depth estimation with traditional visual odometry | Andraghetti | | 2019 | S | | ✓ | ✓ | ✓ |
| 121 | LiStereo: Generate Dense Depth Maps from LIDAR and Stereo Imagery | Zhang | | 2020 | S | | ✓ | x | x |
| 122 | Online Adaptation through Meta-Learning for Stereo Depth Estimation | Zhang | | 2019 | S | | x | x | x |
| 123 | Bilateral Cyclic Constraint and Adaptive Regularization for Unsupervised Monocular Depth Prediction | Wong | | 2019 | M | | ✓ | x | ✓ |
| 124 | Real-time self-adaptive deep stereo | Tonioni | | 2019 | S | | ✓ | ✓ | x |
| 125 | Geometry meets semantics for semi-supervised monocular depth estimation | Ramirez | | 2018 | M | | ✓ | ✓ | ✓ |
| 126 | Open-World Stereo Video Matching with Deep RNN | Zhong | | 2018 | S | | ✓ | x | x |
| 127 | Self-Supervised Learning for Stereo Matching with Self-Improving Ability | Zhong | | 2017 | S | | ✓ | x | x |